JACS
JOURNAL OF THE AMERICAN CHEMICAL SOCIETY
Communication
pubs.acs.org/JACS

In Situ Electrochemical X-ray Absorption Spectroscopy of Oxygen Reduction Electrocatalysis with High Oxygen Flux

Evan M. Erickson,[†] Matthew S. Thorum,[†] Relja Vasić,[‡] Nebojša S. Marinković,[§] Anatoly I. Frenkel,*[,‡] Andrew A. Gewirth,*[,†] and Ralph G. Nuzzo*[,†]

[†]Department of Chemistry, University of Illinois at Urbana-Champaign, Urbana, Illinois 61801, United States
[‡]Physics Department, Yeshiva University, New York, New York 10016, United States
[§]Center for Catalytic Science and Technology, University of Delaware, Newark, Delaware 19716, United States

Supporting Information

ABSTRACT: An in situ electrochemical X-ray absorption spectroscopy (XAS) cell has been fabricated that enables high oxygen flux to the working electrode by utilizing a thin poly(dimethylsiloxane) (PDMS) window. This cell design enables in situ XAS investigations of the oxygen reduction reaction (ORR) at high operating current densities greater than 1 mA in an oxygen-purged environment. When the cell was used to study the ORR for a Pt on carbon electrocatalyst, the data revealed a progressive evolution of the electronic structure of the metal clusters that is both potential-dependent and strongly current-dependent. The trends establish a direct correlation to d-state occupancies that directly tracks the character of the Pt−O bonding present.

The slow kinetics of the oxygen reduction reaction (ORR) and the large overpotential (~300 mV) in fuel cell cathodes necessitate the use of high loadings of precious-metal electrocatalysts for practical applications.[1] The limited supply of Pt and its cost are impediments to the widespread application of fuel cells and air-cathode batteries in automotive and stationary power implementations.[2] The detailed mechanism of the ORR on Pt is still the subject of considerable effort, which makes catalyst design to eliminate the high ORR overpotential uncertain.[1,3] Most ORR mechanistic studies have focused on and usefully characterized adsorption intermediates without monitoring the catalyst evolution specifically.[4−8] Correlation of ORR turnover rates with the electronic and physical characteristics of various materials results in "volcano plots" with highest activity centered around platinum and its alloys.[1,9] This relationship of activity to d-band vacancies and catalyst−oxide bond lengths and strengths follows from structure−property/structure−rate correlations established by the application of the Sabatier principle of heterogeneous catalysis.[1,9] X-ray absorption spectroscopy (XAS) provides a direct means to explore such relationships; d-band occupancy and catalyst oxidation state may be empirically resolved from the X-ray absorption near-edge structure (XANES) region, while coordination number, metal−metal bond distance, metal−oxide bond distance, and their mean-squared disorder may be derived from electron backscattering calculations in the extended X-ray absorption fine structure (EXAFS).[10,11]

In situ XANES studies of Pt established a potential dependence of d-band vacancies.[12] Later, a similar increase in white-line intensity of the Pt L_3 edge concomitant with potential for Pt binary alloys was observed; mass transfer limitations of the cell design, however, precluded measurements at high operating rates.[13,14]

Non-electrochemical studies of metal−adsorbate interactions have shown that small changes in oxidant/reductant concentrations can strongly affect the surface and electronic structure of nanoparticles.[15−20] Understanding the change in the Pt surface during the ORR over a broad operating *IV* range would considerably extend our knowledge of this important electrocatalytic process. Previously, XANES studies of the ORR in the electrochemical environment could not investigate the effect of added O_2 on the Pt structure because of the design of the in situ electrochemical cell, which limited the electrolyte volume, reducing gas saturation of the electrolyte.[10,21−23] As the ORR proceeded, O_2 was consumed and not easily replaced because of poor permeation through the cell materials. One early in situ study attempted the ORR while measuring XAS, but poor O_2 flux limited the studies to high potentials and a comparison of O_2-saturated and O_2-free environments was not included.[23]

In this report, we describe results from a new cell design that removes restrictions in the O_2 supply to the electrode. High oxygen flux is supplied to the working electrode (WE) by using a thin poly(dimethylsiloxane) (PDMS) membrane for the window material. PDMS is a polymer that we have utilized extensively in microfuel cell designs because of its high permeability toward oxygen.[24−28] Figure 1 is a brief schematic showing how the cell was fabricated [for a detailed description, see Figure S1 in the Supporting Information (SI)]. Two PDMS membranes microstructured using soft lithographic techniques[28] were adhered to each other around a Nafion membrane through UV ozone treatment followed by heating (Figure 1A). The microstructure was a pillared arcade, used to prevent adhesion of the PDMS to the Nafion membrane (Figure 1B). The process of forming the PDMS membrane with a sacrificial bulk layer for handling is described in more detail in the Figure S1. The sacrificial bulk layers were carefully peeled away (Figure 1C). The top of the adhered PDMS layers was cut away to make a pouch with two chambers separated by the Nafion

Received: November 7, 2011
Published: December 15, 2011

   dx.doi.org/10.1021/ja210465x | J. Am. Chem.Soc. 2012, 134, 197−200

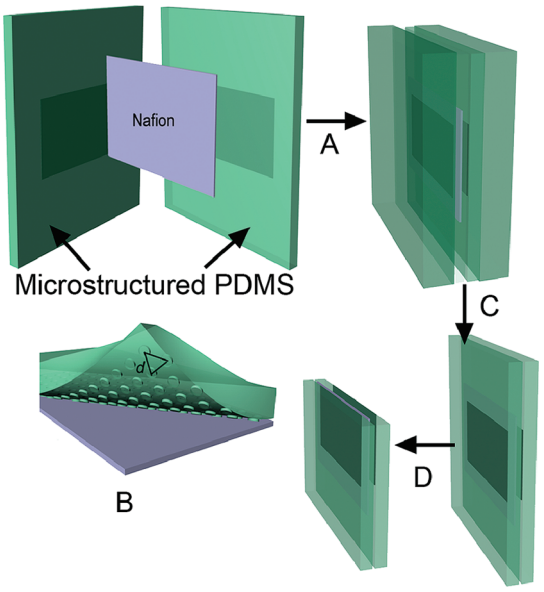

Figure 1. Fabrication of the PDMS pouch used for the XAS cell. (A) To form the pouch, two sides of microsctructured PDMS were cut off the master, treated with ozone, and permanently adhered around Nafion by heating the sample under compression. (B) The microstructured PDMS was in the form of a hexagonal pillared arcade (pillars separated by d = 150 μm) that prevented adhesion of the PDMS to the Nafion. (C) The sacrificial bulk PDMS layers were carefully removed. (D) The top was cut with a razor blade to expose the internal pouch with two chambers separated by Nafion. Full details of the fabrication process are given in the Figure S1.

membrane (Figure 1D). This pouch contained the electrolyte, with the WE and counter electrode (CE) separated by the Nafion membrane (Figure 2A). A photograph of the thin

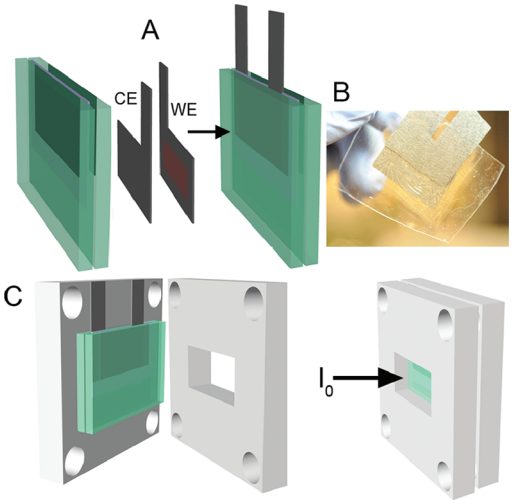

Figure 2. Assembly of the cell with compression plates. (A) The carbon paper counter electrode (CE) and carbon paper/Pt working electrode (WE) were added to the pouch. (B) The PDMS pouch was very thin (~200 μm) and highly permeable to O_2. (C) Teflon compression plates were used to hold the pouch in place, with the whole assembly attached to the flow cell box (Figure S2). Electrolyte was supplied by injection tubing (not shown).

pouch cell is shown in Figure 2B; the thin PDMS membrane provides a large oxygen flux to the WE. Teflon tubing was placed into each chamber of the cell to provide electrolyte; this tubing was fed out of the cell flow box to a syringe with the plungers removed, which was used to supply electrolyte and as a reservoir for the reference electrode. The flow box (Figure S2) was used to control the gas environment. The cell was held together with Teflon compression plates (Figure 2C). The plates were screwed into the flow box with the X-ray windows on the cell and the flow box aligned to allow transmission of the incident beam (I_0).

An airbrush was used to deposit catalyst onto the WE prior to its insertion into the cell.[29,30] A transmission electron microscopy image of the catalyst and its size distribution are shown in Figure S3. The catalyst loading was estimated as 1.8 mg of Pt/cm^2 using Micro CT (Figure S4).

The electrochemical performance of the cell operating in different gas regimes is depicted in Figure 3. All potentials are

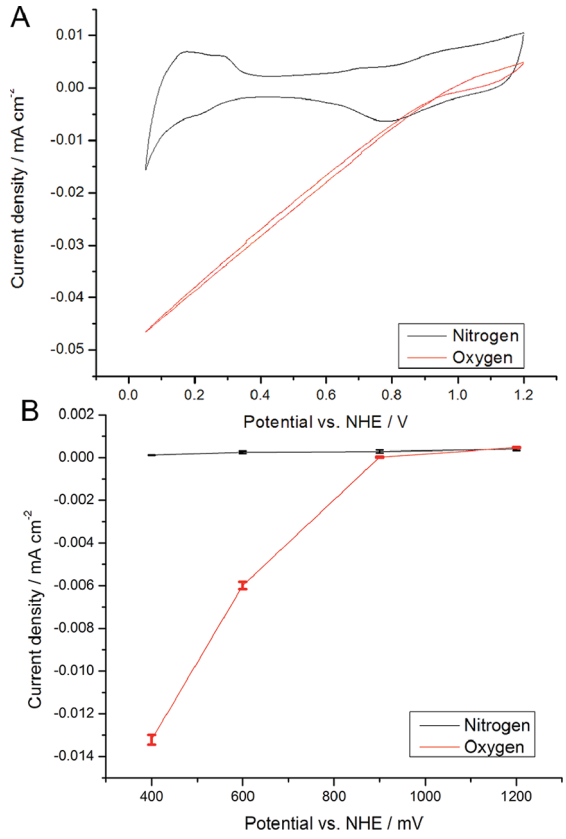

Figure 3. (A) CVs of the electrode in N_2 and O_2 during operation of the in situ electrochemical XAS cell, obtained in 0.1 M $HClO_4$ at 5 mV/s. (B) Corresponding limiting current densities of the electrode under O_2 and N_2, taken from averages over the XAS acquisition times. Error bars are used to mark data points, with lines drawn as a guide. Both used electrochemical surface area in the calculation of the current density, found from the H_2 underpotential deposition region.

referred to the normal hydrogen electrode (NHE), calibrated by flooding with the cell with H_2 prior to experiments. Figure 3A shows cyclic voltammograms (CVs) of the cell in pure O_2- and N_2-purged environments. The CV obtained in the N_2 environment is consistent with that reported previously for Pt dispersed on a carbon support.[31] In the presence of O_2, the onset of cathodic current associated with the ORR occurred at ~0.9 V, and no limiting current density was observed, indicating that O_2 depletion was not occurring. Further electrochemical operating characteristics of the cell are

dx.doi.org/10.1021/ja210465x | J. Am. Chem.Soc. 2012, 134, 197–200

described the SI, including the electrochemical surface area calculation, resistance and capacitive components of the cell, and the gas response of its operation (Figures S5−S8).

XAS experiments were performed at beamline X19A of the National Synchrotron Light Source at Brookhaven National Laboratory. Before XAS measurements, the cell was held for at least 5 min to reach a pseudosteady state; this time was longer for 1.2 V, where oxidation into the bulk occurs. The resultant stable currents are plotted in Figure S5. The current densities were obtained by averaging the cell current during the ~35 min XAS data acquisition period, with the errors determined as standard deviations (Figure 3B). Stable ORR operation was obtained from the ORR onset to at least 400 mV. Acquisition potentials were chosen to be in the Pt oxide region (1.2 V), near the onset potential of the ORR (0.9 V), and in the double-layer region (0.6 and 0.4 V), where adventitious adsorption reactions do not compete with the ORR.

Pt L_3-edge XANES normalized absorbance spectra, $\mu(E)$, presented in Figures 4 and S9 show the potential and O_2 effects on the white line. Figure 4A shows plots of $\Delta\mu(E) = \mu_V(E) - \mu_{V_0}(E)$, the difference between the XANES at potential V under different atmospheres and that at potential V_0 = 400 mV under N_2. The white line of the O_2-exposed electrode (dashed lines) is more intense than that found with N_2 exposure (solid lines) at all potentials. Figure S9 depicts the normalized XANES data for all of the curves shown in Figure 4A.

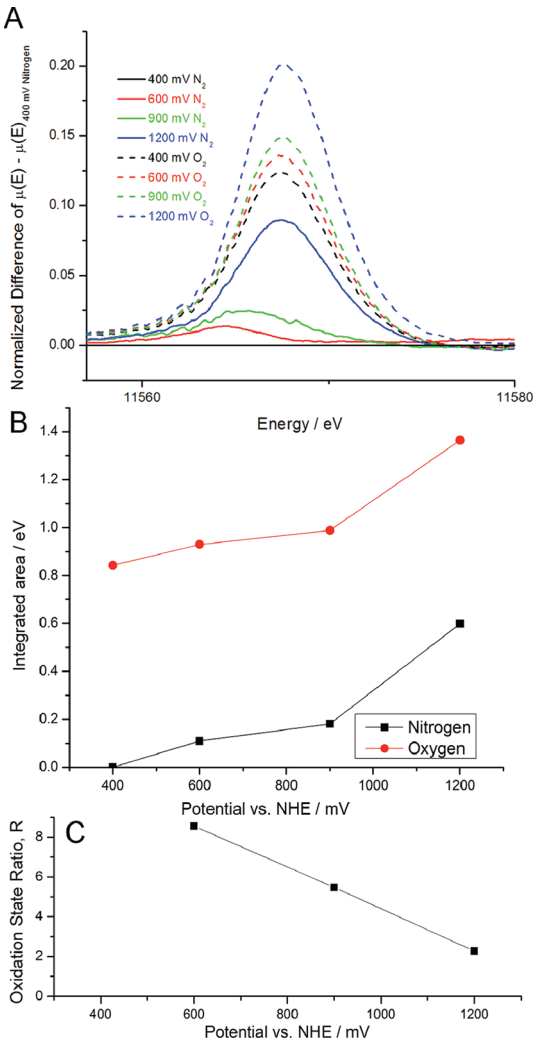

Figure 4. (A) XANES difference ($\Delta\mu$) plots of the electrode at varied potentials under O_2 and N_2, calculated by subtracting the XANES values at 400 mV under N_2 from each white line region. (B) Integrated areas of the spectra in (A), which are directly related to the oxidation state by eq 1, plotted vs potential.[33] (C) Plot of oxygen/nitrogen oxidation state ratio R (calculated from eq 2) vs potential.

The Pt L_3 white-line area is proportional to the density of unoccupied Pt d states and hence can be used to estimate the charge on Pt.[11,32,33] Figure 4B represents the integrated area ΔA, of $\Delta\mu(E)$ for each potential and atmosphere. If it is assumed that the metal is fully reduced (i.e., $Z = 0$) at V_0 = 400 mV in a N_2 environment, the oxidation state at each potential, Z_V, can be found from the following relationship:

$$\Delta A = CZ_V \quad (1)$$

where C is a scaling coefficient.[33] Although we cannot determine absolute oxidation states of Pt at different potentials (since the charge state of Pt at 1.2 V under O_2 cannot be assumed to be fully oxidized,[34] C cannot be obtained by interpolation between the two known oxidation states of Pt), we can quantitatively measure relative changes in oxidation state using eq 1 and Figure 4B at different potentials.

The three main reasons for increases in d-band vacancy and XANES data intensity are a potential increase, electrochemical oxidation of Pt, and O_2 adsorption with subsequent electron donation from Pt. If the relationship in eq 1 is assumed to hold, at all potentials the catalyst under oxygen has a higher oxidation state, suggesting adsorption of oxygen on the surface and resultant adsorbate-mediated electron density transfer. The difference in this oxidation state was roughly equal over all potentials except at 1200 mV, suggesting a constant adsorbed layer of oxidative species below 900 mV. This was further confirmed by the lack of an observed limiting current density in Figure 3; the high oxygen flux toward the WE through the PDMS window provided sufficient flux that the adsorbed layer of oxygen species did not diminish, at least in the level of electron density donated from the Pt d band.

It is interesting to note that even at 1200 mV, the sample under N_2 has a lower oxidation state than that under O_2. The data show that even at this high potential, where oxygen reduction does not occur, there is an effect from adsorbed oxygen. The effect that oxygen has at 1.2 V was explored in Figure S10, which shows that when the working electrode was held at 1.2 V, flooding the electrolyte with oxygen did not increase the area of the electrochemical Pt oxide stripping peak once the system was nitrogen-purged. This suggests that although O_2 adsorption was observed with the XANES measurements at 1.2 V, it predominately involved physisorption; otherwise, a larger Pt oxide reduction peak would have occurred in the CV after flooding with oxygen. This is sensible because the onset potential where oxygen reduction begins (0.9 V) is much lower in potential.

There is an increase in the slope in Figure 4B for both N_2 and O_2 between 900 and 1200 mV. This increase is likely due to oxidation into the bulk, resulting in a larger white line for both curves. The slopes for N_2 and O_2 are not the same, however; the difference between the oxidation states of oxygen and nitrogen decreases with increasing potential (Table S1). The effect appears subtly over the whole potential range as white-line stabilization under O_2, resulting in a greater decrease in oxidation state under N_2 (15% larger than for O_2 over the whole potential range). At 1200 mV, the oxidation state rises more dramatically under N_2 than O_2. This stabilization of the

dx.doi.org/10.1021/ja210465x | J. Am. Chem.Soc. 2012, 134, 197−200

oxidation state under O_2 could be due to three factors. First, at 1200 mV, the surface is electrochemically oxidized, eliminating a portion of sites available for oxygen adsorption and subsequent electron donation. Second, the transition from O_2-reducing potentials between 400−900 mV to nonreducing potentials at 1200 mV also represents a transition from a predominately chemisorbed to predominately physisorbed O_2, resulting in a lower-than-expected increase in the white-line intensity. Third, a portion of the Pt oxide could remain even at lower potentials upon exposure to O_2.

According to the CV in Figure 3A, the platinum should be fully reduced below 600 mV. Thus, the differences in the white lines below this potential are solely due to oxygen adsorption, and the reduction in the white line under N_2 is due to the lowering of the electrochemical potential. At 600 mV, however, the difference between the N_2 and O_2 white-line areas is less than that at 400 mV. This could represent an increasingly physisorbed (vs chemisorbed) presence of oxygen, which results in lower currents as observed in Figure 4B.

This diminishing difference between oxidation states with increased potential can be further illustrated by defining R, the ratio of the oxidation states at a given potential (eq 2):

$$R = \Delta A_{O_2}/\Delta A_{N_2} \quad (2)$$

Figure 4C shows that R decreases with increasing potential. This reduction in R further illustrates that the metal under O_2 is more different from that under N_2 when Pt is ORR-active. The fact that $R(V)$ appears to be linear suggests a smooth transition between the Pt surface with different oxygen activities.

The white-line XANES data show a clear distinction in the electronic structure of the Pt when it reduces oxygen. Electronic differences are normally accompanied by physical differences (e.g., metal−metal bond length, coordination number, and particle size). The error in the EXAFS obtained from these data was too large to derive these physical differences unambiguously. Our ongoing work focuses on improving the instrumental/data collection attributes that currently limit the signal-to-noise character of the EXAFS data. Further studies could utilize the high oxygen flux provided by the cell to focus on other metals to monitor physical and electronic trends in relation to reduction activity.

■ ASSOCIATED CONTENT

Supporting Information

Cell fabrication and operation, experimental procedures, and additional experimental results. This material is available free of charge via the Internet at http://pubs.acs.org.

■ AUTHOR INFORMATION

Corresponding Author

anatoly.frenkel@yu.edu; agewirth@illinois.edu; r-nuzzo@illinois.edu

■ ACKNOWLEDGMENTS

This work was based on funding provided by the U.S. DOE (Grant DE-FG02-05ER46260). A.I.F. and R.G.N. acknowledge support by the U.S. DOE (Grant DE-FG02-03ER15476). Beamline X19A at the NSLS is supported in part by the Synchrotron Catalysis Consortium (U.S. DOE Grant DE-FG02-05ER15688). The authors thank Brad Lutz and Jim Brownfield for fabrication of the box and help with design; Fikile Brushett for help with initial catalyst deposition; and Stoyan Bliznakov, Kotaro Sasaki, and the Adžić group for providing electrolyte, a potentiostat, and help at BNL.

■ REFERENCES

(1) Gewirth, A. A.; Thorum, M. S. *Inorg. Chem.* **2010**, *49*, 3557.
(2) Gasteiger, H. A.; Kocha, S. S.; Sompalli, B.; Wagner, F. T. *Appl. Catal., B* **2005**, *56*, 9.
(3) Fernandez, J. L.; Walsh, D. A.; Bard, A. J. *J. Am. Chem. Soc.* **2005**, *127*, 357.
(4) Murthi, V. S.; Urian, R. C.; Mukerjee, S. *J. Phys. Chem. B* **2004**, *108*, 11011.
(5) Tada, M.; Murata, S.; Asakoka, T.; Hiroshima, K.; Okumura, K.; Tanida, H.; Uruga, T.; Nakanishi, H.; Matsumoto, S.; Inada, Y.; Nomura, M.; Iwasawa, Y. *Angew. Chem., Int. Ed.* **2007**, *46*, 4310.
(6) Teliska, M.; Murthi, V. S.; Mukerjee, S.; Ramaker, D. E. *J. Electrochem. Soc.* **2005**, *152*, A2159.
(7) Wakisaka, M.; Suzuki, H.; Mitsui, S.; Uchida, H.; Watanabe, M. *Langmuir* **2009**, *25*, 1897.
(8) Wakisaka, M.; Udagawa, Y.; Suzuki, H.; Uchida, H.; Watanabe, M. *Energy Environ. Sci.* **2011**, *4*, 1662.
(9) Greeley, J.; Stephens, I. E. L.; Bondarenko, A. S.; Johansson, T. P.; Hansen, H. A.; Jaramillo, T. F.; Rossmeisl, J.; Chorkendorff, I.; Nørskov, J. K. *Nat. Chem.* **2009**, *1*, 552.
(10) Russell, A. E.; Rose, A. *Chem. Rev.* **2004**, *104*, 4613.
(11) Mansour, A. N.; Cook, J. W.; Sayers, D. E. *J. Phys. Chem.* **1984**, *88*, 2330.
(12) Herron, M. E.; Doyle, S. E.; Pizzini, S.; Roberts, K. J.; Robinson, J.; Hards, G.; Walsh, F. C. *J. Electroanal. Chem.* **1992**, *324*, 243.
(13) Mukerjee, S.; Srinivasan, S.; Soriaga, M. P.; McBreen, J. *J. Electrochem. Soc.* **1995**, *142*, 1409.
(14) Mukerjee, S.; Srinivasan, S.; Soriaga, M. P.; McBreen, J. *J. Phys. Chem.* **1995**, *99*, 4577.
(15) Sanchez, S. I.; Menard, L. D.; Bram, A.; Kang, J. H.; Small, M. W.; Nuzzo, R. G.; Frenkel, A. I. *J. Am. Chem. Soc.* **2009**, *131*, 7040.
(16) Tao, F.; Grass, M. E.; Zhang, Y.; Butcher, D. R.; Renzas, J. R.; Liu, Z.; Chung, J. Y.; Mun, B. S.; Salmeron, M.; Somorjai, G. A. *Science* **2008**, *322*, 932.
(17) Yoshitake, H.; Iwasawa, Y. *J. Phys. Chem.* **1991**, *95*, 7368.
(18) Yoshitake, H.; Iwasawa, Y. *J. Phys. Chem.* **1992**, *96*, 1329.
(19) Peng, H.; Krauss, T. D.; Miller, B. L. *Anal. Chem.* **2010**, *82*, 8664.
(20) Small, M. W.; Sanchez, S. I.; Menard, L. D.; Kang, J. H.; Frenkel, A. I.; Nuzzo, R. G. *J. Am. Chem. Soc.* **2011**, *133*, 3582.
(21) Herron, M. E.; Doyle, S. E.; Roberts, K. J.; Robinson, J.; Walsh, F. C. *Rev. Sci. Instrum.* **1992**, *63*, 950.
(22) Mathew, R. J.; Russell, A. E. *Top. Catal.* **2000**, *10*, 231.
(23) Weber, R. S.; Peuckert, M.; Dallabetta, R. A.; Boudart, M. *J. Electrochem. Soc.* **1988**, *135*, 2535.
(24) Erickson, E. M.; Mitrovski, S. M.; Gewirth, A. A.; Nuzzo, R. G. *Electrophoresis* **2011**, *32*, 947.
(25) Mitrovski, S. M.; Elliott, L. C. C.; Nuzzo, R. G. *Langmuir* **2004**, *20*, 6974.
(26) Mitrovski, S. M.; Nuzzo, R. G. *Lab Chip* **2005**, *5*, 634.
(27) Mitrovski, S. M.; Nuzzo, R. G. *Lab Chip* **2006**, *6*, 353.
(28) Xia, Y. N.; Whitesides, G. M. *Angew. Chem., Int. Ed.* **1998**, *37*, 551.
(29) Paganin, V. A.; Ticianelli, E. A.; Gonzalez, E. R. *J. Appl. Electrochem.* **1996**, *26*, 297.
(30) Sun, L.; Ran, R.; Wang, G.; Shao, Z. *Solid State Ionics* **2008**, *179*, 960.
(31) Higuchi, E.; Uchida, H.; Watanabe, M. *J. Electroanal. Chem.* **2005**, *583*, 69.
(32) Lytle, F. W.; Wei, P. S. P.; Greegor, R. B.; Via, G. H.; Sinfelt, J. H. *J. Chem. Phys.* **1979**, *70*, 4849.
(33) Yoshida, H.; Nonoyama, S.; Yazawa, Y.; Hattori, T. *Phys. Scr.* **2005**, *T115*, 813.
(34) Vetter, J.; Schultze, J. W. *J. Electroanal. Chem.* **1972**, *34*, 131.